Journal of MATERIALS RESEARCH

Article
DOI: 10.1557/jmr.2019.248

BUILDING ADVANCED MATERIALS VIA PARTICLE AGGREGATION AND MOLECULAR SELF-ASSEMBLY

FOCUS ISSUE

3-Dimensional graphene/Cu/Fe_3O_4 composites: Immobilized laccase electrodes for detecting bisphenol A

Congqiang Lou[1], Tao Jing[1,a)], Jingzhi Tian'[1], Yongjie Zheng[1,b)], Jiaoxia Zhang[2,c)], Mengyao Dong[3], Chao Wang[1], Chuanxin Hou[4], Jincheng Fan[5], Zhanhu Guo[6,d)]

[1]*School of Chemistry and Chemical Engineering, Qiqihar University, Qiqihar, Heilongjiang Province 161000, China*
[2]*School of Materials Science and Engineering, Jiangsu University of Science and Technology, Zhenjiang 212003, China*
[3]*Key Laboratory of Materials Processing and Mold (Zhengzhou University), Ministry of Education, National Engineering Research Center for Advanced Polymer Processing Technology, Zhengzhou University, Zhengzhou 450001, China*
[4]*Integrated Composites Laboratory (ICL), Department of Chemical & Biomolecular Engineering, University of Tennessee, Knoxville, Tennessee 37996, USA; and School of Materials Science and Engineering, North University of China, Taiyuan 030051, China*
[5]*College of Materials Science and Engineering, Changsha University of Science and Technology, Changsha 410114, China*
[6]*Integrated Composites Laboratory (ICL), Department of Chemical & Biomolecular Engineering, University of Tennessee, Knoxville, Tennessee 37996, USA*

[a)]Address all correspondence to these authors. e-mail: jtkr@163.com
[b)]e-mail: zyj1964@163.com
[c)] e-mail: zhangjx@just.edu.cn
[d)]e-mail: zguo10@utk.edu

Received: 29 April 2019; accepted: 17 July 2019

Three-dimensional graphene (3D-GN)/Cu/Fe_3O_4 composite support materials were synthesized by a modified chemical reduction method using graphene oxide precursor. A 3D-GN/Cu/Fe_3O_4 biosensor was prepared by coating the electrode with laccase. The electrochemical properties of the biosensor were investigated by cyclic voltammetry (CV) and differential pulse voltammetry using potassium ferricyanide, phosphate-buffered saline (PBS) solution, and bisphenol A (BPA) solution. The current response of 3D-GN/Cu/Fe_3O_4 biosensors presents a remarkable sensitivity based on CV. The linear range of BPA is 7.2–18 μM using differential pulse voltammetry in PBS solution (pH = 4.0). A linear fitting equation of the laccase biosensor was observed for the current response as a function of BPA concentration. The detection limit was decreased to 1.7 μM. The detection approach herein turns out to be highly sensitive, has a wide linear range, and exhibits excellent stability.

Introduction

With the continuous progress of industrialization and increasing demands of new materials [1, 2, 3, 4, 5, 6, 7, 8, 9, 10, 11, 12, 13] and energy [14, 15, 16, 17, 18, 19, 20, 21, 22, 23, 24, 25, 26, 27, 28, 29, 30], serious pollution of environment is caused by the release of many chemicals such as heavy metals [31, 32, 33, 34, 35], organics [36, 37, 38], gases [39, 40], and oils that are harmful to animals and plants [41, 42, 43, 44, 45]. Environmental estrogen or endocrine disruptor (EDC) is an important pollutant [46]. After entering the human body, it has two main effects on human beings. Firstly, it competes with the body's own estrogen to bind serum protein, affecting the normal functions of its own estrogen. Secondly, its binding to nuclear receptors affects the hormonal homeostasis [46]. Bisphenol A (BPA), namely, 2,2-bis-(4-hydroxyphenyl)propane, as the endocrine disruptor, has been widely used as an industrial raw material for synthesizing polymers such as food packaging and medical materials. However, the large-scale use of BPA brings great harms to human life by interfering with the human endocrine system, affecting fertility as well as immune functions, and increasing the risk of cancer [47]. The traditional methods for detecting BPA, including high-performance liquid chromatography [48], gas chromatography–mass spectrometry [49], and fluorescence method [50], have their disadvantages such as inaccurate measurement and difficult control. By contrast, electrochemical methods have received extensive attention because of their high sensitivity, simple instrumentation, high responsiveness, potential for miniaturization, and in situ analysis.

Electrochemical sensors [51, 52, 53] possess the characteristics of simple operation, low cost, fast analysis speed, high

https://doi.org/10.1557/jmr.2019.248 Published online by Cambridge University Press

© The Authors 2019

sensitivity, and online analysis. They are of great interest in environmental testing, food industry, biomedical research, and fermentation industrial production [54, 55, 56, 57]. To better detect BPA via the electrochemical method, various nanomaterials and nanocomposites have been used to modify the bare electrode. Among lots of nanomaterials, graphene attracts much attention because of its unique planar and lamellar crystal structure nowadays. Graphene presents to be a high specific surface area and the ordered and long-order π bond structure delivers the excellent thermal conductivity [52, 58], electrical conductivity [52, 59], and biocompatibility [60, 61], being suitable for various applications, e.g., energy storage, catalysis, sensing, and biology [62, 63, 64, 65, 66, 67, 68, 69, 70, 71, 72, 73]. Furthermore, graphene holds a great promise to be an ideal electrical sensor support material [74, 75, 76, 77, 78] such as graphene-based H_2O_2 sensor [68], DNA sensor [69], dopamine sensor [70], and glucose sensor [74]. Metal nanoparticles (NPs) with their large specific surface areas and some unique chemical and physical properties also exhibit excellent catalytic respondence [79, 80, 81, 82]. Cu NPs prepared based on chemical reduction of copper(II) nitrate trihydrate possessed the 10^{-8} M of detection limits for BPA, outstanding stability and repeatability [83]. The three-dimensional Cu-MOF exhibited a great prospect for sensitive and rapid detection of BPA because of the p–p stacking interactions between BPA and Cu-MOF [84]. Unfortunately, the metal NPs with their high specific surface areas and surface energy tend to aggregate together, resulting in decreasing the catalytic respondence. Therefore, it is necessary to anchor metal NPs to some supporters to decrease the agglomeration and enhance their stability. Two-dimensional nanomaterials and porous materials show great advantages. In addition, Fe_3O_4 NPs have been attractive because of their low level of toxicity, superparamagnetism, and biocompatibility. The Fe_3O_4 decorated with chitosan to reduce the agglomeration tendency displayed the sensitive electrochemical determination of BPA with the limit of detection of 8.0×10^{-9} mol/dm^3 [47].

The electrochemical enzyme biosensors have both molecular and selective recognition catalytic functions of enzymes, while rapidly measuring the concentration of target substances. They feature a sensitive detection, easy operation, and rapid chemical reaction [48, 85, 86, 87, 88, 89]. Therefore, in this work, to prevent the agglomerate tendency of nanomaterials and exploit the synergistic effect, the Cu and Fe_3O_4 NPs were decorated to the surface of 3D-GN by a modified chemical reduction method. A laccase biosensor was prepared by coating the 3D-GN/Cu/Fe_3O_4 with laccase to measure the BPA content in a liquid. Functional graphene composites can provide active sites for enzymatic reactions with a high conductivity. Laccase has been used as a molecular recognition unit, with a low specificity of the substrate, mild reaction conditions, and simple operation. The graphene composite–modified electrode was synthesized through the modified chemical reduction protocol. The current response of graphene composites was analyzed by cyclic voltammetry (CV), and the detection limit of enzyme biosensor was measured by differential pulse voltammetries. The biosensor used to detect the BPA content features a low detection limit, wide linear range, and high selectivity, and can be used for detecting the content in tap water samples.

Results and discussion

Characterization of electrode materials

Firstly, 3D-GO/GCE, 3D-GN/Cu/GCE, and 3D-GN/Cu/Fe_3O_4/GCE were characterized by Fourier transform infrared (FI-IR) to check the chemical structure (see Fig. 1). For the 3D-GO spectrum [Fig. 1(a)], the absorption peak at 1017 cm^{-1} denotes the C–O–C stretching, the absorption peak at 3423 cm^{-1} represents the O–H stretching, and the stretching vibration absorption peak at C=O is 1622 cm^{-1}. The spectrum of 3D-GN/Cu [Fig. 1(b)] and 3D-GN/Cu/Fe_3O_4 [Fig. 1(c)] shows that the absorptive oxygen-containing functional groups are reduced. This indicates that 3D-GO is reduced to 3D-GN. The absorption peak of 569 cm^{-1} in 3D-GN/Cu/Fe_3O_4 corresponds to the stretching vibration of Fe–O, indicating the presence of Fe_3O_4.

The 3D-GN/Cu/Fe_3O_4 composites were characterized by transmission electron microscopy (TEM) and scanning electron microscope (SEM) (Fig. 2) to observe the microstructure and morphology. It can be clearly seen from the SEM image [Fig. 2(a)] that the graphene exhibits the stable fold and wrinkles and the Cu and Fe_3O_4 NPs are uniformly decorated on the surface of graphene. The TEM image [Fig. 2(b)] further displays the layer structure, and 3D graphene presents

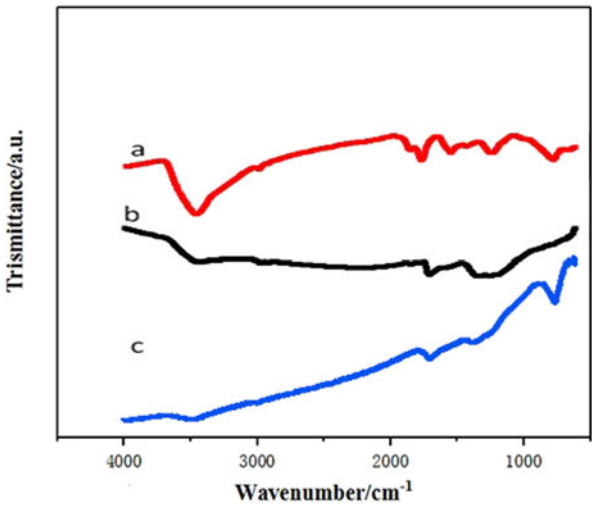


Figure 1: Infrared spectra of composites: (a) 3D-GO, (b) 3D-GN/Fe_3O_4, and (c) 3D-GN/Cu/Fe_3O_4.

https://doi.org/10.1557/jmr.2019.248 Published online by Cambridge University Press

© The Authors 2019

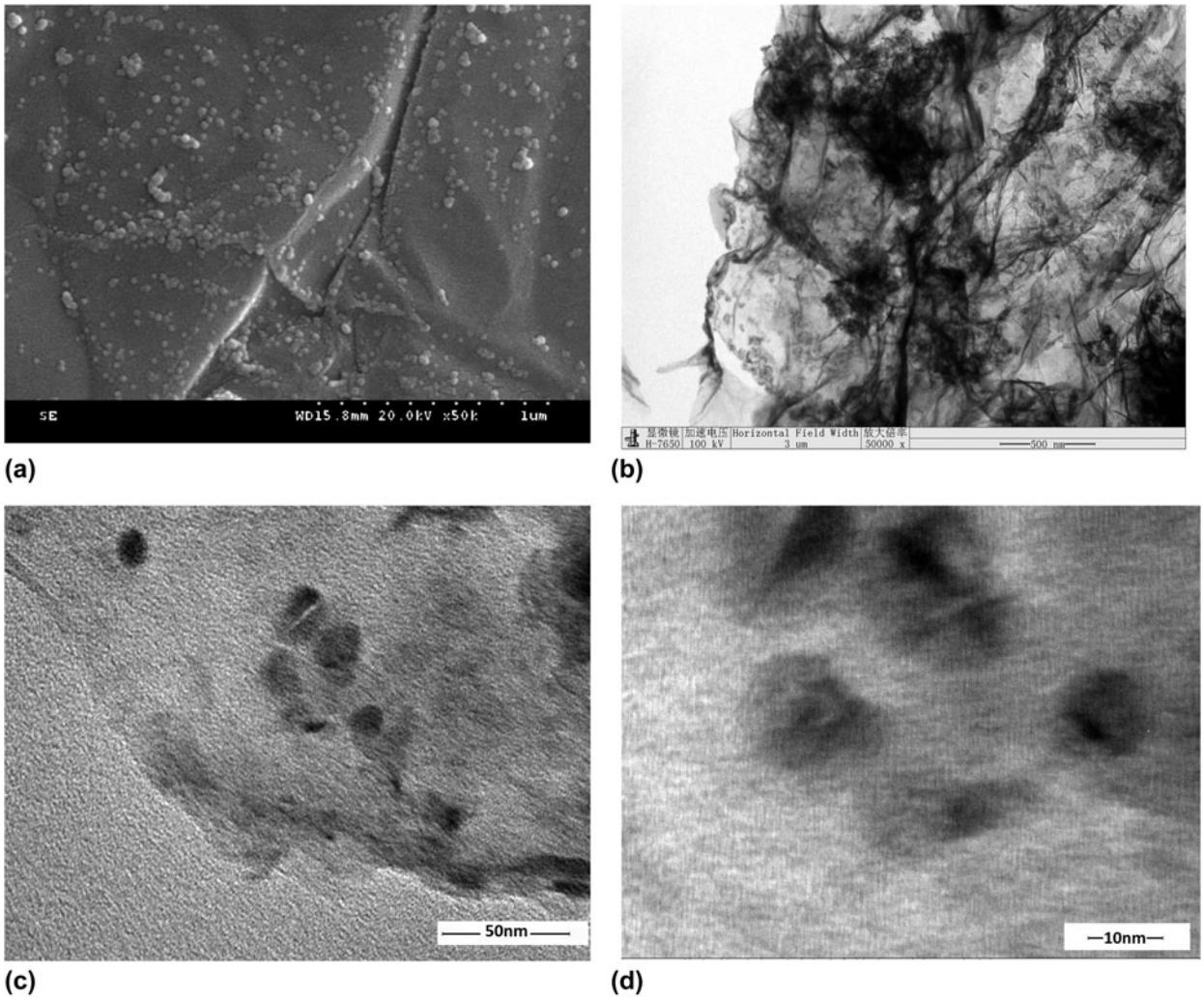


Figure 2: (a) SEM, (b) TEM, and (c) and (d) HRTEM images of 3D-GN/Cu/Fe_3O_4.

a three-dimensional skeleton structure. The edge sheets are thin and transparent. This indicates that the 3D graphene is single or few layers. These properties provide a good environment for further loading NPs. Figure 2(b) also demonstrates that the NPs supported without agglomeration on the graphene sheets are evenly distributed and their particle size distribution is about 15 nm. It can be seen that the layered structure of the composites have wrinkles from the HRTEM [Figs. 2(c) and 2(d)], which prove the three-dimensional structure of graphene and uniform dispersion of the NPs on the surface. The diameter of the Cu NPs is between 10 and 30 nm, and the added Fe_3O_4 NPs have no obvious agglomeration phenomenon, which proves that the dispersibility is good.

The component of the sample was investigated by XRD. As shown in Fig. 3, the broad peak observed from 20 to 28° was attributed to the diffraction of graphene. The three peaks at 43.5, 50.5, and 74.5° in the range of 40–80° can be assigned to the diffraction from the (111), (200), and (220) planes of Cu(0) with a cubic phase, respectively. The peaks at $2\theta = 18.9°$, 30.2°, 35.5°, 57.2°, and 62.9° can be, respectively, indexed to (111), (200), (311), (400), (511), and (400) diffractions of Fe_3O_4. From Fig. 3, it can be seen that the component was successfully prepared.

The 3D-GN/Cu/Fe_3O_4/GCE is further characterized by X-ray photoelectron spectroscopy (XPS) to check the element and valence state. Figure 4(a) is the full spectrum of the XPS of 3D-GN/Cu/Fe_3O_4 composites, and Figs. 4(b)–4(d) are the high-resolution spectra of Fe 2*p*, Cu 2*p*, and C 1*s*, respectively. Besides C and O elements, Fe 2*p* can be seen from the full spectrum [Fig. 4(a)]. The peaks of Cu 2*p* appeared at 710 and 935 eV. The high-resolution spectrum of Fe 2*p* [Fig. 4(b)] reveals the two peaks at 711.2 and 725.6 eV, corresponding to Fe $2p_{3/2}$ and Fe $2p_{1/2}$, respectively. The peak about 720 eV (corresponding to γ-Fe_2O_3) is not observed, indicating that only Fe_3O_4 is present in the electrode and is not oxidized [31]. The two peaks at 933.3 and 953.7 eV correspond to Cu $2p_{3/2}$ and Cu $2p_{1/2}$, respectively, for the spectrum of Cu 2*p* [Fig. 4(c)], indicating the presence of

https://doi.org/10.1557/jmr.2019.248 Published online by Cambridge University Press

© The Authors 2019

Cu. In addition, the two weak peaks at about 945 and 964 eV (corresponding to Cu^{2+}) indicate the residual Cu^{2+} in the 3D-GN/Cu/Fe_3O_4/GCE. There is a strong C–C signal at 284.3 eV, a weak C–O signal at 286.8 eV, and an O–C=O signal at 288.6 eV, implying a partial reduction of GO. So, the main component of prepared sample is 3D-GN/Cu/Fe_3O_4.

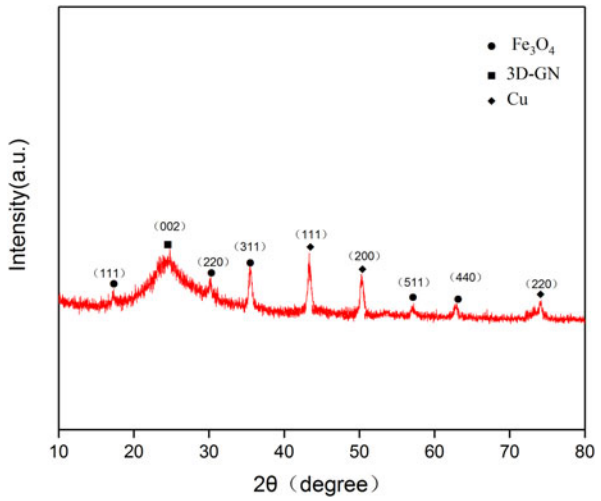


Figure 3: XRD spectra of 3D-GN/Cu/Fe_3O_4 composites.

Electrochemical behavior of the modified electrode

The CV test for GCE, 3D-GN/GCE, 3D-GN/Cu/GCE, and 3D-GN/Cu/Fe_3O_4/GCE was performed in the range of −0.6–0.6 V, and the sweep speed of 1 mV/s was executed in a 0.10 mol/L KNO_3 solution containing 5.0×10^{-3} mol/L $K_3Fe(CN)_6$ (see Fig. 5). From Fig. 4, the CV curves for all samples show a clear redox peak, and the redox peaks all are symmetrical. The peak current ratio is about 1:1, and the voltage difference is less than 200 mV, confirming that the electron transport between the carrier and the electrode is stable. The current response on the electrode is normal, and the reaction is reversible.

By comparing the electrochemical response of bare electrode in the solution [Fig. 5(a)] and that of the 3D-GN material coated on the surface of the bare GCE [Fig. 4(b)], the later has a reversible oxidation peak at −0.22 V with a peak current of

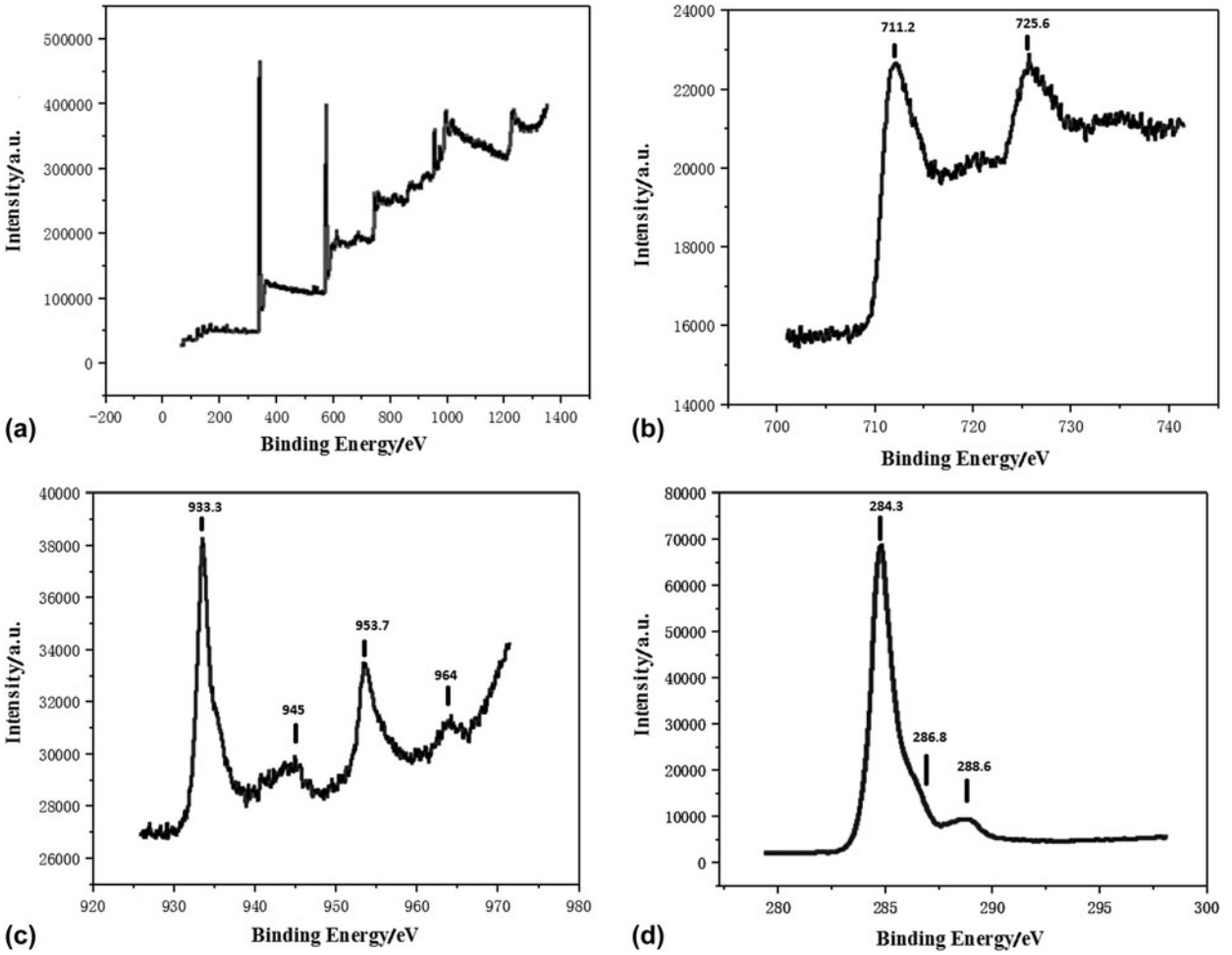


Figure 4: (a) XPS spectrum of 3D-GN/Cu/Fe_3O_4 composites, (b) Fe 2*p* spectrum of 3D-GN/Cu/Fe_3O_4/composites, (c) Cu 2*p* spectrum of 3D-GN/Cu/Fe_3O_4 composites, and (d) C 1*s* spectrum of 3D-GN/Cu/Fe_3O_4 composites.

https://doi.org/10.1557/jmr.2019.248 Published online by Cambridge University Press

© The Authors 2019

0.359 μA. Moreover, the 3D-GN/Cu/GCE [Fig. 5(c)] shows a reversible reduction peak at −0.17 V with a peak current of 0.489 μA. The loading of Cu improves the catalytic activity and the conductivity of the 3D-GN/GCE. When the 3D-GN/Cu/Fe_3O_4/GCE is prepared by mixing Fe_3O_4 NPs in the 3D-GN/Cu material, the peak current of the oxidation current of the electrode is −0.22 V, and the peak current increases to 0.684 μA, indicating that the redox process of the 3D-GN/Cu/Fe_3O_4/GCE has a higher activity [Fig. 5(d)]. Both Fe_3O_4 NPs and 3D-GN/Cu exhibit a high electrochemical activity, and these two materials are simultaneously introduced into the electrode surface to exert a synergistic effect. Besides, the 3D-GN material facilitates the dispersion of NPs. As a good electronic media, Cu and Fe_3O_4 increase the electron transfer rate and can effectively enhance the conductivity of the electrode. In addition, the high specific surface area of 3D-GN effectively expands the electrochemical effective surface area of the electrode, which makes more electrolyte contact the electrode surface to enhance the response signal, so that the 3D-GN/Cu/Fe_3O_4/GCE shows a higher electrochemical activity.

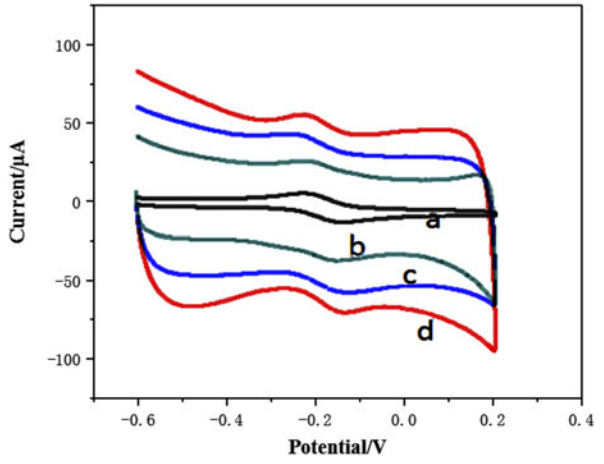


Figure 5: CV of different modified electrodes: (a) bare electrodes, (b) 3D-GN/GCE, (c) 3D-GN/Cu/GCE, and (d) 3D-GN/Cu//Fe_3O_4/GCE.

Dynamic performance

The laccase solution was loaded onto the 3D-GN/Cu/Fe_3O_4/GCE by the dipping method. The relationship between the potential scanning rate (V) and the electrochemical behavior of BPA was investigated by CV. The Lac-3D-GN/Cu/Fe_3O_4/GCE biosensor was tested in pH 4.0 phosphate-buffered saline (PBS) and with a potential range of −0.6–0.2 V. Figure 6 shows that the square root of the sweep speed was linear to the peak current. The linear equation follows: $I = 4.36 + 82.1v^{1/2}$ (V/s) 1/2, $r = 0.9973$. A larger sweep speed indicates a higher peak current. The reaction of BPA on the modified electrode is a surface control process. As the sweep rate increases, it is also confirmed that the enzyme activity remains remarkable.

Effect of solution pH

CV was used to study the electrical behavior of the solution pH of BPA in the PBS buffer solution (Fig. 7). The oxidation peak current first increases and then decreases in the range of pH 3–7. At pH 4.0, the maximum oxidation peak current occurs in the PBS solution. As the pH increases, the oxidation peak current gradually decreases until the enzyme electrode has no catalytic activity at pH 7.0. This can be ascribed to the hydroxyl and cyanide interfered with the oxygen molecules at the active site, which result in the loss of the electrocatalytic activity of laccase. It is proved that the catalytic activity of the enzyme is the best when the pH of the PBS buffer solution is 4.0. In the range of pH 3–7, the oxidation peak potential of the electrode gradually shifts negatively with increasing the pH because the protons participate in the electrode reaction and has a linear

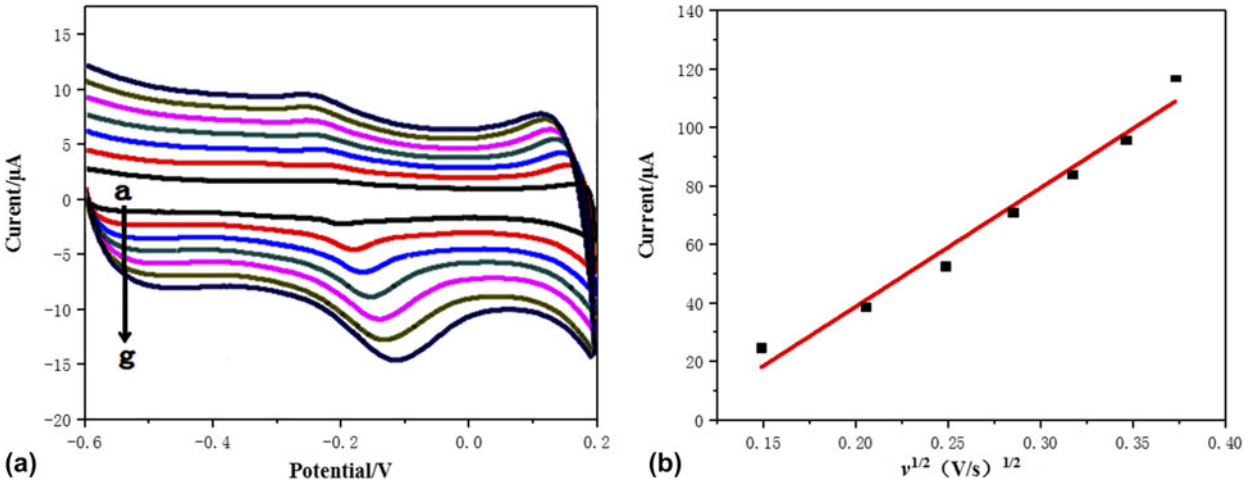


Figure 6: (a) CV of Lac-3D-GN/Cu/Fe_3O_4 biosensor at sweep speeds of 20, 40, 60, 80, 100, 120, and 140 mV/s (from a to g), and (b) the relationship between Lac-3D-GN/Cu/Fe_3O_4 biosensor sweep speed and peak current.

https://doi.org/10.1557/jmr.2019.248 Published online by Cambridge University Press

© The Authors 2019

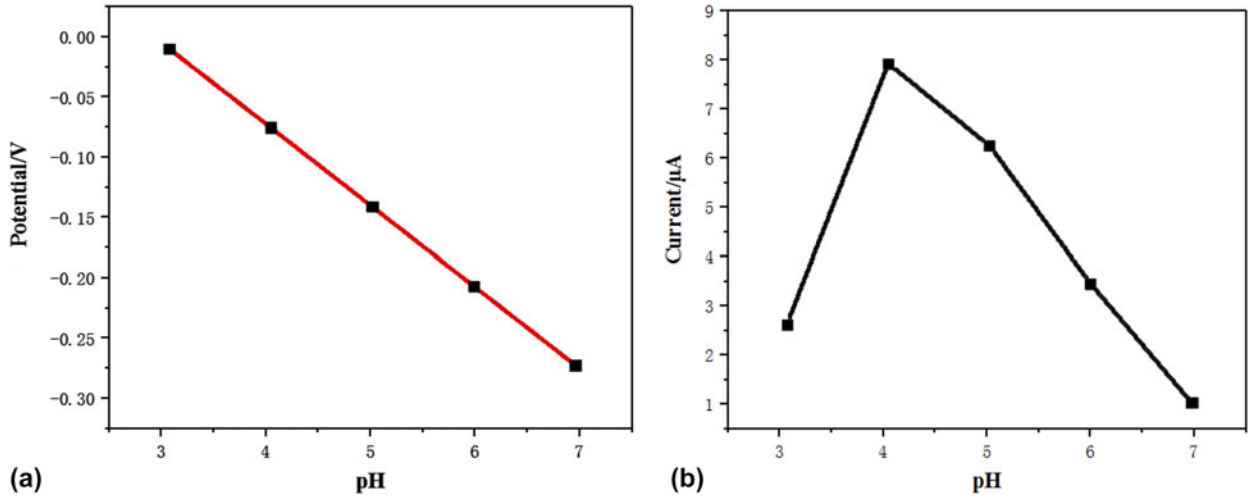


Figure 7: Relationship between potential and pH (a) and current value and pH (b) of Lac-3D-GN/Cu/Fe_3O_4/GCE biosensor in a 0.2 M citric acid buffer solution of pH 3–7.

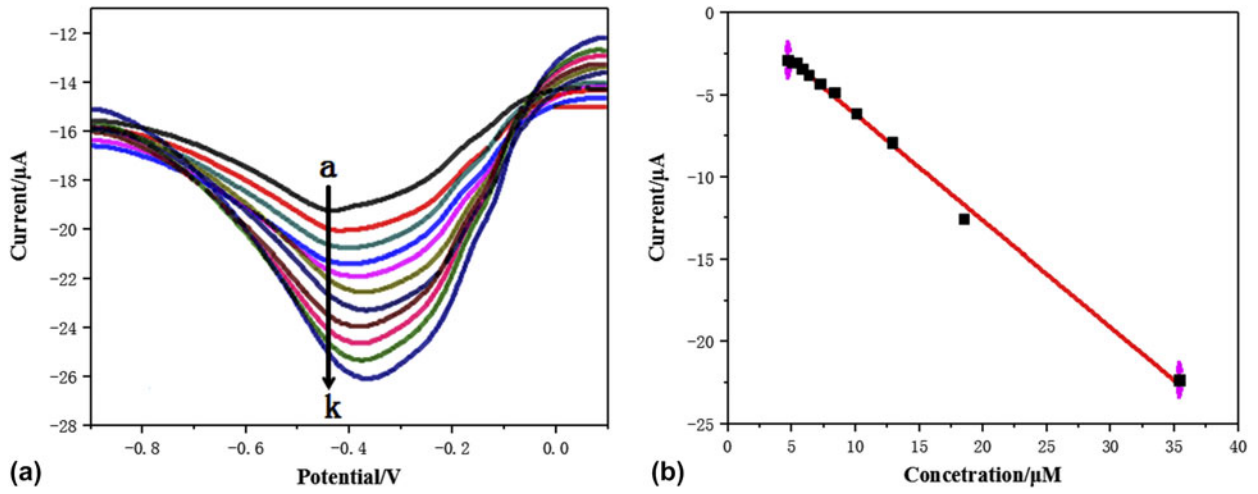


Figure 8: (a) Differential pulse curve of Lac-3D-GN/Cu/Fe_3O_4/GCE biosensor at different concentrations of BPA of pH 4.0 (a–k: 3.3, 3.6, 4, 4.5, 5.1, 6, 7.2, 9, 12, 18, and, 36 μmol/L) and (b) the relationship between Lac-3D-GN/Cu/Fe_3O_4//GCE biosensor concentration and peak current.

relationship with pH. The linear equation is as follows: E = 0.2018–0.0686 pH, r = −0.9964, indicating that BPA underwent four electron transfers and had four proton transfers.

Differential pulse voltammetry for determining the BPA content

Linear range and detection limit

Differential pulse voltammetry was applied to determine the BPA content with different concentration gradients at pH = 4.0. Figure 8 shows that the relationship between the peak current of BPA and its concentration is linear in the range of 7.2–18 μmol/L. The linear equation is as follows: $I = -1.0944 \times 10^{-6} - 0.356 \times 10^{-6}c$, the correlation coefficient r = 0.996, and the detection limit is 1.7 μM (S/N = 3). Compared with the biosensor prepared by Dempsey et al. [78], this biosensor has a considerable detection limit and a wide linear range. This biosensor is equivalent to the biosensor prepared by Portaccio et al. [86] because of the excellent carrier effect of 3D-GN, resulting in obtaining NPs with small particle size and uniform dispersion.

Reproducibility of biosensor

The reproducibility of biosensor test was performed by differential pulse voltammetry with a BPA solution of 7.2 μmol/L. Three Lac-3D-GN/Cu/Fe_3O_4/GCE biosensors were prepared under the identical conditions, and the same test was carried out in the same solution system [Fig. 9(a)]. The three curves were found to be close and almost identical, and the peak value was unchanged. The measured standard deviation of the peak current was 6.3%, indicating the high reproducibility of the biosensors.

https://doi.org/10.1557/jmr.2019.248 Published online by Cambridge University Press

© The Authors 2019

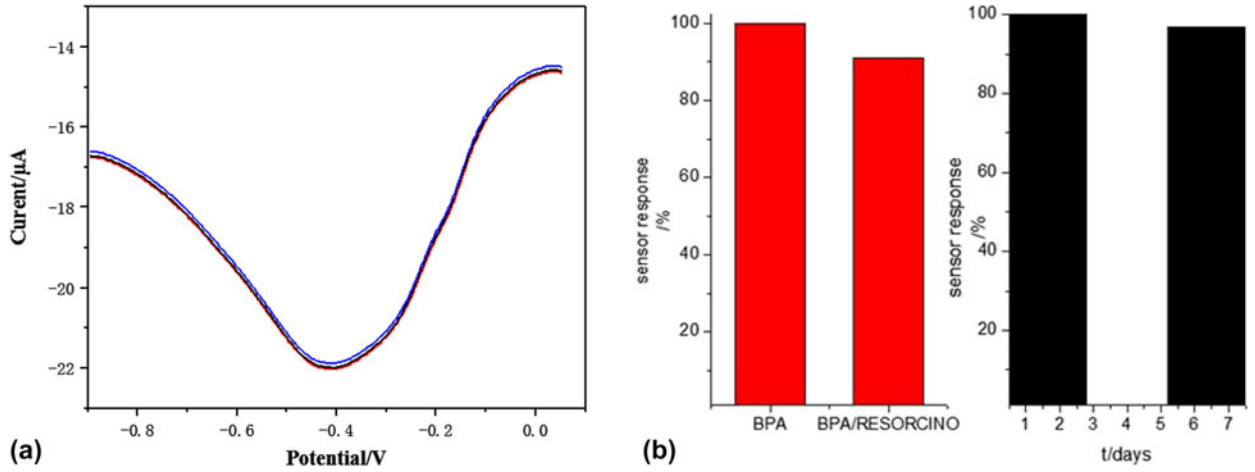


Figure 9: (a) Reproducibility of Lac-3D-GN/Cu/Fe_3O_4/GCE biosensor and (b) anti-interference and storage stability of Lac-3D-GN/Cu/Fe_3O_4/GCE biosensor.

TABLE I: Determination of BPA content in tap water samples.

Sample	Real value μmol/L	Detection value μmol/L	Recovery %	Relative standard deviation %
1	4.5	4.5157	100.3	7
...	...	4.0607	90.23	...
...	...	4.0607	103.6	...
...	...	4.0124	89.16	...
...	...	4.4370	98.6	...

Anti-interference and stability

Differential pulse voltammetry was used to test the change in the current response before and after adding the interfering substances. 0.5 g *m*-diphenol was added to a BPA solution with a concentration of 7.2 μmol/L at pH 4.0. The current response to BPA was 100% before adding the interfering substances. The responsivity of the current was 91.1% after adding resorcinol [Fig. 9(b)]. The biosensor was found to have a strong anti-interference ability and selectivity to BPA. The laccase biosensor was placed at 4 °C for one week at a pH of 4.0 and the change in the current response was tested with a BPA concentration of 7.2 μmol/L via differential pulse voltammetry. The current response after one week was 98.9%. Laccase had a good biological activity on the biosensors. The laccase biosensor has an acceptable storage stability.

Water sample test

The water sample was taken from laboratory running water, and the pH of tap water was adjusted to 4.0. It was continuously measured five times, and the relative standard deviation (RSD) of the measurement results was 7%. The measured value and the true value were calculated from the linear relationship between the current and the concentration in Fig. 7. The recovery test of sample water was carried out, and the recovery rate was obtained (Table I). The recovery rate was between 96 and 102%. Therefore, the biosensor was found to have an excellent testability for BPA in the actual samples and could be used to detect the concentration of BPA in nature.

Conclusions

The prepared 3D-GN/Cu/Fe_3O_4 composites present a remarkable dispersibility, large specific surface area, and adequate active sites. The physical and chemical properties of the electrode are obviously improved. The excellent conductivity and uniform dispersion and synergistic effect of Fe_3O_4 NPs, Cu, and 3D-GN facilitate the electrochemical activity. The resulted composite materials can be widely used as an excellent carrier to enhance the performance of electrochemical biosensors. The Lac-3D-GN/Cu/Fe_3O_4/GCE had an excellent laccase activity. At pH 4.0, the detection of BPA has a low detection limit, wide linear range, and excellent selectivity. The reproducibility, selectivity, and stability of the biosensor are turned out to be extraordinary. The detection of real water samples is only 7% RSD, indicating the adaptability to determine the BPA content in nature. These materials combining the conductive copper and graphene and the magnetic magnetite have potential applications for other fields such as electromagnetic interference (EMI) shielding [90, 91, 92] and strain sensors [79, 93, 94, 95].

Experimental section

Materials

Analytically pure BPA was obtained from Tianjin Kemi Chemical Reagent Co., Ltd. (Tianjin, China), natural flake graphite was purchased from Qingdao Jinrilai Graphite Co.,

https://doi.org/10.1557/jmr.2019.248 Published online by Cambridge University Press

© The Authors 2019

Ltd. (Qingdao, China), and laccase was supplied by Cool Biotechnology Co., Ltd. (Fuyang, China). Potassium permanganate ($KMnO_4$), copper sulfate ($CuSO_4$) powder, absolute ethanol, sodium nitrate, sodium citrate, natrium aceticum, hydrogen peroxide, and hydrazine hydrate were obtained from Kemi Ou Chemical Reagent Co., (Tianjin, China). The other reagents used in the experiment were analytically pure, and the solution was formulated using ultrapure water.

The synthesis of 3D-GO, 3D-GN, and Fe_3O_4

Three-dimensional graphene oxide (3D-GO) and graphene (3D-GN) were prepared by methods described previously [70]. Briefly, 5 g natural flake graphite, 3 g sodium nitrate, and 120 mL concentrated H_2SO_4 were gradually added into the absolute dry flask and stirred to disperse completely the mixture in ice-water bath (10–15 °C). 20 g $KMnO_4$ were slowly added into the above mixture to stir for 2 h at 15 °C. The mixture was continued to stir for half an hour at 35 °C, 2 min at 98 °C, and then cooled to room temperature. The hydrogen peroxide was added dropwise into the mixture to remove excess $KMnO_4$. The dilute hydrochloric acid and warm deionized water were used to wash until the pH value of solution was close to neutral. The obtained product was dispersed in ultrapure water and ultrasonic treated for 1 h, and then freeze-dried to obtain 3D-GO. The reducing agent hydrazine hydrate was added in to 100 mL GO (0.05 g/L) water solution and stirred for 24 h at 60 °C. The mixture was flushed and filtrated by ethanol and ultrapure water for several times. After being freeze-dried, the sample was collected, which was named as 3D-GN.

The hydrothermal method was used to prepare Fe_3O_4 NPs (Fe_3O_4 NPs). The 2.2 g $FeCl_3{\cdot}6H_2O$ was completely dissolved in 80 mL ethylene glycol. Then, natrium aceticum and sodium citrate mixture was added to the above solution. The colloidal solution was transferred in to hydrothermal reactor and heat-treated at 200 °C for 20 h to obtain Fe_3O_4 NPs.

The synthesis of electrode materials

For preparing 3D graphene/copper (3D-GN/Cu) composites, 0.040 g of 3D-GO was mixed with ultrapure water and placed in an ultrasonic cleaner to ultrasonically dissolve the clear and nonparticulate matter in the solution. Furthermore, 0.012 g of copper sulfate powder was weighed and put into the suspension prepared in the first step. The reducing agent sodium borohydride solution was slowly added dropwise as the solution changed from dark brown to black, and then heated in a water bath at 80 °C for 4 h. The prepared 3D-GN/Cu was washed with water until the pH was neutral and kept for further use. Then, the treated Fe_3O_4 NPs were added to the prepared 0.012 g of 3D-GN/Cu solution by simple physical mixing based on the ultrasonic treatment to obtain a 3D-GN/Cu/Fe_3O_4 composite material, which was freeze-dried and collected for further use.

The electrode was treated before decoration as follow. The glassy carbon electrode (GCE, Φ = 3 mm) was continuously polished with α-Al_2O_3 powder (particle size is 10, 0.3, and 0.05, respectively) until mirror surface was formed. The polished electrode was rinsed with water and HNO_3–H_2O solution [HNO_3:H_2O = 1:1 (volume ratio)], and ultrasonic cleaned for 3 min. Then, the electrode was dipped in 0.5 mol/L H_2SO_4 and cyclic scanned until the current maintained stable at 100 mV/s sweep speed and at −0.6 to ~0.2 V potential range. The electrode was then rinsed with ultrapure water and the surface of the electrode was blow-dried with nitrogen for further use.

The aforementioned 3D-GN, 3D-GN/Cu, and 3D-GN/Cu/Fe_3O_4 composite materials were separately dispersed in the solution, dropped on the surface of the above electrode (GCE), and dried naturally. The modified electrode was represented as 3D-GN/GCE, 3D-GN/Cu/GCE, and 3D-GN/Cu/Fe_3O_4/GCE, respectively. The laccase electrode Lac-3D-GN/Cu/Fe_3O_4/GCE was prepared by dripping the laccase buffer solution on the 3D-GN/Cu/Fe_3O_4/GCE.

Characterization of electrode materials

The dispersibility, surface morphology, and spatial structure of the electrode materials were observed by transmission electron microscopy (TEM) (Hitachi S-7650, Tokyo, Japan), and scanning electron microscope (SEM) (Hitachi S-4300, Tokyo, Japan). The surface composition and valence state were analyzed by Thermo Scientific K-Alpha X-ray photoelectron spectroscopy (XPS) (Thermo Fisher, Waltham, Massachusetts). The surface chemistry of the electrode materials was examined by Fourier transform infrared (FT-IR) (PE Spectrum One B FTIR, PerkinElmer, Hopkinton, Massachusetts) based on KBr tablet from 500 to 4000 cm^{-1}.

Electrochemical tests

A CHI 660C electrochemical workstation (CH Instruments, Shanghai, China) was employed via a three-electrode system: modified GCE, namely, electrode materials as the working electrode, Pt electrode as the counter electrode, and saturated Ag/AgCl electrode as the reference electrode. Electrochemical tests were conducted to obtain CV curve. For GCE, 3D-GN/GCE, 3D-GN/Cu/GCE, and 3D-GN/Cu/Fe_3O_4/GCE, the 0.10 mol/L KNO_3 solution containing 5.0×10^{-3} mol/L $K_3Fe(CN)_6$ was used as electrolyte solution for the CV test at the range of −0.6–0.6 V and at the sweep speed of 1 mV/s. For Lac-3D-GN/Cu/Fe_3O_4 biosensor, PBS and 0.10 mol/L KNO_3 solution contain BPA at different sweep speeds. PBS was obtained with

https://doi.org/10.1557/jmr.2019.248 Published online by Cambridge University Press

© The Authors 2019

0.1 mol/L Na_2HPO_4 and 0.1 mol/L NaH_2PO_4 in different proportions.

Acknowledgments

The authors are grateful for the Project supported by the Graduate innovation research projects for Qiqihar University (Item No.: YJSCX2018-030X).

References

1. **L. Ma, Y. Zhu, M. Wang, X. Yang, G. Song, and Y. Huang**: Enhancing interfacial strength of epoxy resin composites via evolving hyperbranched amino-terminated POSS on carbon fiber surface. *Compos. Sci. Technol.* **170**, 148 (2019).
2. **L. Ma, N. Li, G. Wu, G. Song, X. Li, P. Han, G. Wang, and Y. Huang**: Interfacial enhancement of carbon fiber composites by growing TiO_2 nanowires onto amine-based functionalized carbon fiber surface in supercritical water. *Appl. Surf. Sci.* **433**, 560 (2018).
3. **L. Ma, Y. Zhu, P. Feng, G. Song, Y. Huang, H. Liu, J. Zhang, J. Fan, H. Hou, and Z. Guo**: Reinforcing carbon fiber epoxy composites with triazine derivatives functionalized graphene oxide modified sizing agent. *Composites, Part B* **176**, 107078 (2019).
4. **G. Zhu, X. Cui, Y. Zhang, S. Chen, M. Dong, H. Liu, Q. Shao, T. Ding, S. Wu, and Z. Guo**: Poly(vinyl butyral)/graphene oxide/poly (methylhydrosiloxane) nanocomposite coating for improved aluminum alloy anticorrosion. *Polymer* **172**, 415 (2019).
5. **J. Yang, W. Yang, X. Wang, M. Dong, H. Liu, E.K. Wujcik, Q. Shao, S. Wu, T. Ding, and Z. Guo**: Synergistically toughening polyoxymethylene by methyl methacrylate–butadiene–styrene copolymer and thermoplastic polyurethane. *Macromol. Chem. Phys.* **220**, 1800567 (2019).
6. **Z. Lin, B. Lin, Z. Wang, S. Chen, C. Wang, M. Dong, Q. Gao, Q. Shao, T. Ding, H. Liu, S. Wu, and Z. Guo**: Facile preparation of 1T/2H–$Mo(S_{1-x}Se_x)_2$ nanoparticles for boosting hydrogen evolution reaction. *ChemCatChem* **11**, 2217 (2019).
7. **H. Gu, X. Xu, M. Dong, P. Xie, Q. Shao, R. Fan, C. Liu, S. Wu, R. Wei, and Z. Guo**: Carbon nanospheres induced high negative permittivity in nanosilver-polydopamine metacomposites. *Carbon* **147**, 550 (2019).
8. **Z.J. Shi, G.F. Xu, J. Deng, M.Y. Dong, V. Murugadoss, C.T. Liu, Q. Shao, S.D. Wu, and Z.H. Guo**: Structural characterization of lignin from *D. sinicus* by FTIR and NMR techniques. *Green Chem. Lett. Rev.* **12**, 235 (2019).
9. **G. Xu, Z. Shi, Y. Zhao, J. Deng, M. Dong, C. Liu, V. Murugadoss, X. Mai, and Z. Guo**: Structural characterization of lignin and its carbohydrate complexes isolated from bamboo (*Dendrocalamus sinicus*). *Int. J. Biol. Macromol.* **126**, 376 (2019).
10. **Z. Shi, C. Jia, D. Wang, J. Deng, G. Xu, C. Wu, M. Dong, and Z. Guo**: Synthesis and characterization of porous tree gum grafted copolymer derived from *Prunus cerasifera* gum polysaccharide. *Int. J. Biol. Macromol.* **133**, 964 (2019).
11. **Z. Zhao, P. Bai, R.D.K. Misra, M. Dong, R. Guan, Y. Li, J. Zhang, L. Tan, J. Gao, T. Ding, W. Du, and Z. Guo**: AlSi10Mg alloy nanocomposites reinforced with aluminum-coated graphene: Selective laser melting, interfacial microstructure and property analysis. *J. Alloys Compd.* **792**, 203 (2019).
12. **X. Gong, Y. Liu, Y. Wang, Z. Xie, Q. Dong, M. Dong, H. Liu, Q. Shao, N. Lu, V. Murugadoss, T. Ding, and Z. Guo**: Amino graphene oxide/dopamine modified aramid fibers: Preparation, epoxy nanocomposites and property analysis. *Polymer* **168**, 131 (2019).
13. **Q. Chen, Q. Yin, A. Dong, Y. Gao, Y. Qian, D. Wang, M. Dong, Q. Shao, H. Liu, B-H. Han, T. Ding, Z. Guo, and N. Wang**: Metal complex hybrid composites based on fullerene-bearing porous polycarbazole for H_2, CO_2 and CH_4 uptake and heterogeneous hydrogenation catalysis. *Polymer* **169**, 255 (2019).
14. **X.L. Luo, F. Pei, W. Wang, H.M. Qian, K.K. Miao, Z. Pan, Y.S. Chen, and G.D. Feng**: Microwave synthesis of hierarchical porous materials with various structures by controllable desilication and recrystallization. *Microporous Mesoporous Mater.* **262**, 148 (2018).
15. **Y.C. Liu, M.J. Shi, C. Yan, Q.Q. Zhuo, H.Z. Wu, L. Wang, H. Liu, and Z.H. Guo**: Inspired cheese-like biomass-derived carbon with plentiful heteroatoms for high performance energy storage. *J. Mater. Sci.: Mater. Electron.* **30**, 6583 (2019).
16. **L. Yang, M. Shi, J. Jiang, Y. Liu, C. Yan, H. Liu, and Z. Guo**: Heterogeneous interface induced formation of balsam pear-like PPy for high performance supercapacitors. *Mater. Lett.* **244**, 27 (2019).
17. **Y.Y. Sheng, J. Yang, F. Wang, L.C. Liu, H. Liu, C. Yan, and Z.H. Guo**: Sol–gel synthesized hexagonal boron nitride/titania nanocomposites with enhanced photocatalytic activity. *Appl. Surf. Sci.* **465**, 154 (2019).
18. **X.L. Luo, Z. Pan, F. Pei, Z.P. Jin, K.K. Miao, P.F. Yang, H.M. Qian, Q. Chen, and G.D. Feng**: In situ growth of hollow Cu_2O spheres using anionic vesicles as soft templates. *J. Ind. Eng. Chem.* **59**, 410 (2018).
19. **C. Shen, X. Liu, H. Cao, Y. Zhou, J. Liu, J. Tang, X. Guo, H. Huang, and X. Chen**: Brain-Like navigation scheme based on MEMS-INS and place recognition. *Appl. Sci.* **9**, 1708 (2019).
20. **Z.Y. Zhao, R.G. Guan, J.H. Zhang, Z.Y. Zhao, and P.K. Bai**: Effects of process parameters of semisolid stirring on microstructure of Mg–3Sn–1Mn–3SiC (wt%) strip processed by rheo-rolling. *Acta Metall. Sin.* **30**, 66 (2017).
21. **M. Liu, Z. Yang, H. Sun, C. Lai, X. Zhao, H. Peng, and T. Liu**: A hybrid carbon aerogel with both aligned and interconnected pores as interlayer for high-performance lithium–sulfur batteries. *Nano Res.* **9**, 3735 (2016).

https://doi.org/10.1557/jmr.2019.248 Published online by Cambridge University Press

© The Authors 2019

22. **M.K. Liu, B.M. Li, H. Zhou, C. Chen, Y.Q. Liu, and T.X. Liu**: Extraordinary rate capability achieved by a 3D "skeleton/skin" carbon aerogel-polyaniline hybrid with vertically aligned pores. *Chem. Commun.* **53**, 2810 (2017).
23. **T. Liang, L. Qi, Z. Ma, Z. Xiao, Y. Wang, H. Liu, J. Zhang, Z. Guo, C. Liu, W. Xie, T. Ding, and N. Lu**: Experimental study on thermal expansion coefficient of composite multi-layered flaky gun propellants. *Composites, Part B* **166**, 428 (2019).
24. **R. Ma, Y. Wang, H. Qi, C. Shi, G. Wei, L. Xiao, Z. Huang, S. Liu, H. Yu, C. Teng, H. Liu, V. Murugadoss, J. Zhang, Y. Wang, and Z. Guo**: Nanocomposite sponges of sodium alginate/graphene oxide/polyvinyl alcohol as potential wound dressing: In vitro and in vivo evaluation. *Composites, Part B* **167**, 396 (2019).
25. **J. Ren, Q. Hou, H. Chen, T. Liu, H. He, J. Wang, Q. Shao, M. Dong, S. Wu, N. Wang, J. Lin, Q. Luo, and Z. Guo**: Suppressing charge recombination and ultraviolet light degradation of perovskite solar cells using silicon oxide passivation. *ChemElectroChem* **6**, 3167 (2019).
26. **B. Lin, Z. Lin, S. Chen, M. Yu, W. Li, Q. Gao, M. Dong, Q. Shao, S. Wu, T. Ding, and Z. Guo**: Surface intercalated spherical $MoS_{2x}Se_{2(1-x)}$ nanocatalysts for highly efficient and durable hydrogen evolution reactions. *Dalton Trans.* **48**, 8279 (2019).
27. **K. Le, Z. Wang, F. Wang, Q. Wang, Q. Shao, V. Murugadoss, S. Wu, W. Liu, J. Liu, Q. Gao, and Z. Guo**: Sandwich-like NiCo layered double hydroxide/reduced graphene oxide nanocomposite cathodes for high energy density asymmetric supercapacitors. *Dalton Trans.* **48**, 5193 (2019).
28. **Y. Ma, C. Hou, H. Zhang, Q. Zhang, H. Liu, S. Wu, and Z. Guo**: Three-dimensional core–shell Fe_3O_4/polyaniline coaxial heterogeneous nanonets: Preparation and high performance supercapacitor electrodes. *Electrochim. Acta* **315**, 114 (2019).
29. **R. Li, X. Zhu, Q. Fu, G. Liang, Y. Chen, L. Luo, M. Dong, Q. Shao, C. Lin, R. Wei, and Z. Guo**: Nanosheet-based $Nb_{12}O_{29}$ hierarchical microspheres for enhanced lithium storage. *Chem. Commun.* **55**, 2493 (2019).
30. **M. Idrees, S. Batool, J. Kong, Q. Zhuang, H. Liu, Q. Shao, N. Lu, Y. Feng, E.K. Wujcik, Q. Gao, T. Ding, R. Wei, and Z. Guo**: Polyborosilazane derived ceramics—Nitrogen sulfur dual doped graphene nanocomposite anode for enhanced lithium ion batteries. *Electrochim. Acta* **296**, 925 (2019).
31. **Y. Yuan, Q. Yu, J. Wen, C. Li, Z. Guo, X. Wang, and N. Wang**: Ultrafast and highly selective uranium extraction from seawater by hydrogel-like spidroin-based protein fiber. *Angew. Chem., Int. Ed.* **58**, 11785 (2019).
32. **S. Li, P. Yang, X. Liu, J. Zhang, W. Xie, C. Wang, C. Liu, and Z. Guo**: Graphene oxide based dopamine mussel-like cross-linked polyethylene imine nanocomposite coating with enhanced hexavalent uranium adsorption. *J. Mater. Chem. A.* **7**, 16902 (2019).
33. **Y. Huang, X. Zeng, L. Guo, J. Lan, L. Zhang, and D. Cao**: Heavy metal ion removal of wastewater by zeolite-imidazolate frameworks. *Sep. Purif. Technol.* **194**, 462 (2018).
34. **Z. Zhao, H. An, J. Lin, M. Feng, V. Murugadoss, T. Ding, H. Liu, Q. Shao, X. Mai, N. Wang, H. Gu, S. Angaiah, and Z. Guo**: Progress on the photocatalytic reduction removal of chromium contamination. *Chem. Rec.* **19**, 873 (2019).
35. **Y.X. Qian, Y.H. Yuan, H.L. Wang, H. Liu, J.X. Zhang, S. Shi, Z.H. Guo, and N. Wang**: Highly efficient uranium adsorption by salicylaldoxime/polydopamine graphene oxide nanocomposites. *J. Mater. Chem. A* **6**, 24676 (2018).
36. **Z. Guo, P. Yang, L. Yang, Q. Luo, J. Wang, Y. hao, R. Yang, X. Lai, X. Zhao, Q. Gao, Q. Shao, S. Wu, T. Ding, Q. fu, X. Mai, M. Dong, and J. Lin**: Anchoring carbon nanotubes and post-hydroxylation treatment enhanced Ni nanofiber catalysts towards efficient hydrous hydrazine decomposition for an effective hydrogen generation. *Chem. Commun.* **55**, 9011 (2019).
37. **S. Xu, Y. Lv, X. Zeng, and D. Cao**: ZIF-derived nitrogen-doped porous carbons as highly efficient adsorbents for removal of organic compounds from wastewater. *Chem. Eng. J.* **323**, 502 (2017).
38. **H. Sun, Z. Yang, Y. Pu, W. Dou, C. Wang, W. Wang, X. Hao, S. Chen, Q. Shao, M. Dong, S. Wu, T. Ding, and Z. Guo**: Zinc oxide/vanadium pentoxide heterostructures with enhanced day-night antibacterial activities. *J. Colloid Interface Sci.* **547**, 40 (2019).
39. **Z. Shi, C. Wu, Y. Gu, Y. Liang, G. Xu, H. Liu, J. Zhang, H. Hou, J. Zhang, and Z. Guo**: Preparation and characterization of mesoporous CuO/ZSM-5 catalysts for automotive exhaust purification. *Sci. Adv. Mater.* **11**, 1198 (2019).
40. **Y.Z.M. Wang, T. Jing, J. Tian, P. Chen, M. Dong, C. Wang, C. Yan, C. Liu, T. Ding, W. Xie, and Z. Guo**: Component determination and their formation of PM2.5. *Sci. Adv. Mater.* **11**, 756 (2019).
41. **X. Niu, W. Yang, G. Wang, J. Ren, H. Guo, and J. Gao**: A novel electrochemical sensor of bisphenol A based on stacked graphene nanofibers/gold nanoparticles composite modified glassy carbon electrode. *Electrochim. Acta* **98**, 167 (2013).
42. **C-L. Lin, J-X. Zhang, and L. Lan**: Analyses of rural drinking water resources quality in the north area of Shaanxi. *Desalin. Water Treat.* **54**, 637 (2015).
43. **C. Lin, B. Fan, J.X. Zhang, X. Yang, and H. Zhang**: Study on lead ion wastewater treatment of self-assembled film. *Desalin. Water Treat.* **57**, 21627 (2016).
44. **Z. Shi, C. Wu, Y. Wu, H. Liu, G. Xu, J. Deng, H.L.H. Gu, J. Zhang, A. Umar, Y. Ma, and Z. Guo**: Optimization of epoxypinane synthesis by silicotungstic acid supported on SBA-15 catalyst using response surface methodology. *Sci. Adv. Mater.* **11**, 699 (2019).
45. **C. Wang, F. Lan, Z. He, X. Xie, Y. Zhao, H. Hou, L. Guo, V. Murugadoss, H. Liu, Q. Shao, Q. Gao, T. Ding, R. Wei, and Z. Guo**: Iridium-based catalysts for solid polymer electrolyte electrocatalytic water splitting. *ChemSusChem* **12**, 1576 (2019).

https://doi.org/10.1557/jmr.2019.248 Published online by Cambridge University Press

© The Authors 2019

46. **S. Andreescu and O.A. Sadik**: Correlation of analyte structures with biosensor responses using the detection of phenolic estrogens as a model. *Anal. Chem.* **76**, 552 (2004).
47. **C.M. Yu, L.L. Gou, X.H. Zhou, N. Bao, and H.Y. Gu**: Chitosan–Fe_3O_4 nanocomposite based electrochemical sensors for the determination of bisphenol A. *Electrochim. Acta* **56**, 9056 (2011).
48. **S. Chen, J. Chen, and X. Zhu**: Solid phase extraction of bisphenol A using magnetic core–shell (Fe_3O_4@SiO_2) nanoparticles coated with an ionic liquid, and its quantitation by HPLC. *Microchim. Acta* **183**, 1315 (2016).
49. **Y. Sun, W-Y. Zhang, J. Xing, and C-M. Wang**: Solid phase microfibers based on modified single-walled carbon nanotubes for simultaneous determination of alkylphenols and bisphenol A in purified water samples. *Chin. J. Anal. Chem.* **39**, 1432 (2011).
50. **L. Du, C. Zhang, L. Wang, G. Liu, Y. Zhang, and S. Wang**: Ultrasensitive time-resolved microplate fluorescence immunoassay for bisphenol A using a system composed on gold nanoparticles and a europium(III)-labeled streptavidin tracer. *Microchim. Acta* **182**, 539 (2015).
51. **X. Lu, Y. Li, L. Tao, D. Song, Y. Wang, Y. Li, and F. Gao**: Amorphous metal boride as a novel platform for acetylcholinesterase biosensor development and detection of organophosphate pesticides. *Nanotechnology* **30**, 055501 (2019).
52. **Y. Shao, J. Wang, H. Wu, J. Liu, I.A. Aksay, and Y. Lin**: Graphene based electrochemical sensors and biosensors: A review. *Electroanalysis* **22**, 1027 (2010).
53. **Y. Liu, X. Qu, H. Guo, H. Chen, B. Liu, and S. Dong**: Facile preparation of amperometric laccase biosensor with multifunction based on the matrix of carbon nanotubes–chitosan composite. *Biosens. Bioelectron.* **21**, 2195 (2006).
54. **X.L. Luo, A. Morrin, A.J. Killard, and M.R. Smyth**: Application of nanoparticles in electrochemical sensors and biosensors. *Electroanalysis* **18**, 319 (2006).
55. **S. Wu, Q. He, C. Tan, Y. Wang, and H. Zhang**: Graphene-based electrochemical sensors. *Small* **9**, 1160 (2013).
56. **S. Ge, M. Yan, J. Lu, M. Zhang, F. Yu, J. Yu, X. Song, and S. Yu**: Electrochemical biosensor based on graphene oxide-Au nanoclusters composites for L-cysteine analysis. *Biosens. Bioelectron.* **31**, 49 (2012).
57. **S. Ameen, M.S. Akhtar, and H.S. Shin**: Hydrazine chemical sensing by modified electrode based on in situ electrochemically synthesized polyaniline/graphene composite thin film. *Sens. Actuators, B* **173**, 177 (2012).
58. **J. Zhang, P. Li, Z. Zhang, X. Wang, J. Tang, H. Liu, Q. Shao, T. Ding, A. Umar, and Z. Guo**: Solvent-free graphene liquids: Promising candidates for lubricants without the base oil. *J. Colloid Interface Sci.* **542**, 159 (2019).
59. **F. Schwierz**: Graphene transistors: Status, prospects, and problems. *Proc. IEEE* **101**, 1567 (2013).
60. Anonymous: The rise and rise of graphene. *Nat. Nanotechnol.* **5**, 755 (2010).
61. **A.K. Geim and K.S. Novoselov**: The rise of graphene. *Nat. Mater.* **6**, 183 (2007).
62. **C. Hou, Z. Tai, L. Zhao, Y. Zhai, Y. Hou, Y. Fan, F. Dang, J. Wang, and H. Liu**: High performance MnO@C microcages with a hierarchical structure and tunable carbon shell for efficient and durable lithium storage. *J. Mater. Chem. A* **6**, 9723 (2018).
63. **J. Zhang, Z. Zhang, Y. Jiao, H. Yang, Y. Li, J. Zhang, and P. Gao**: The graphene/lanthanum oxide nanocomposites as electrode materials of supercapacitors. *J. Power Sources* **419**, 99 (2019).
64. **J. Xia, F. Chen, J. Li, and N. Tao**: Measurement of the quantum capacitance of graphene. *Nat. Nanotechnol.* **4**, 505 (2009).
65. **Y. Jiao, J. Zhang, S. Liu, Y. Liang, S. Li, H. Zhou, and J. Zhang**: The graphene oxide ionic solvent-free nanofluids and their battery performances. *Sci. Adv. Mater.* **10**, 1706 (2018).
66. **Z. Cheng, Q. Li, Z. Li, Q. Zhou, and Y. Fang**: Suspended graphene sensors with improved signal and reduced noise. *Nano Lett.* **10**, 1864 (2010).
67. **J.X. Zhang, Y.X. Liang, X. Wang, H.J. Zhou, S.Y. Li, J. Zhang, Y. Feng, N. Lu, Q. Wang, and Z. Guo**: Strengthened epoxy resin with hyperbranched polyamine-ester anchored graphene oxide via novel phase transfer approach. *Adv. Compos. Hybrid Mater.* **1**, 300 (2018).
68. **Y. Sun, C. Li, Y. Xu, H. Bai, Z. Yao, and G. Shi**: Chemically converted graphene as substrate for immobilizing and enhancing the activity of a polymeric catalyst. *Chem. Commun.* **46**, 4740 (2010).
69. **D. Chen, H. Zhang, Y. Liu, and J. Li**: Graphene and its derivatives for the development of solar cells, photoelectrochemical, and photocatalytic applications. *Energy Environ. Sci.* **6**, 1362 (2013).
70. **Y. Li, T. Jing, G. Xu, J. Tian, M. Dong, Q. Shao, B. Wang, Z. Wang, Y. Zheng, C. Yang, and Z. Guo**: 3-D magnetic graphene oxide-magnetite poly(vinyl alcohol) nanocomposite substrates for immobilizing enzyme. *Polymer* **149**, 13 (2018).
71. **Y. He, Q. Chen, H. Liu, L. Zhang, D. Wu, C. Lu, W. OuYang, D. Jiang, M. Wu, J. Zhang, Y. Li, J. Fan, C. Liu, and Z. Guo**: Friction and wear of MoO_3/graphene oxide modified glass fiber reinforced epoxy nanocomposites. *Macromol. Mater. Eng.*, 1900166 (2019).
72. **X. Huang, R. Yin, L. Qian, W. Zhao, H. Liu, C. Liu, J. Fan, H. Hou, and Z. Guo**: Processing conditions dependent tunable negative permittivity in reduced graphene oxide-alumina nanocomposites. *Ceram. Int.* **45**, 11784 (2019).
73. **B. Kirubasankar, V. Murugadoss, J. Lin, T. Ding, M. Dong, H. Liu, J. Zhang, T. Li, N. Wang, Z. Guo, and S. Angaiah**: In situ grown nickel selenide on graphene nanohybrid electrodes for high energy density asymmetric supercapacitors. *Nanoscale* **10**, 20414 (2018).
74. **W. Li, X. Geng, Y. Guo, J. Rong, Y. Gong, L. Wu, X. Zhang, P. Li, J. Xu, G. Cheng, M. Sun, and L. Liu**: Reduced graphene oxide electrically contacted graphene sensor for highly sensitive nitric oxide detection. *ACS Nano* **5**, 6955 (2011).

https://doi.org/10.1557/jmr.2019.248 Published online by Cambridge University Press

© The Authors 2019

75. **H.J. Yoon, D.H. Jun, J.H. Yang, Z. Zhou, S.S. Yang, and M.M-C. Cheng**: Carbon dioxide gas sensor using a graphene sheet. *Sens. Actuators, B* **157**, 310 (2011).
76. **B. Zhang and T. Cui**: An ultrasensitive and low-cost graphene sensor based on layer-by-layer nano self-assembly. *Appl. Phys. Lett.* **98**, 073116 (2011).
77. **G.S. Kulkarni, K. Reddy, Z. Zhong, and X. Fan**: Graphene nanoelectronic heterodyne sensor for rapid and sensitive vapour detection. *Nat. Commun.* **5**, 4376 (2014).
78. **H. Choi, J.S. Choi, J-S. Kim, J-H. Choe, K.H. Chung, J-W. Shin, J.T. Kim, D-H. Youn, K-C. Kim, J-I. Lee, S-Y. Choi, P. Kim, C-G. Choi, and Y-J. Yu**: Flexible and transparent gas molecule sensor integrated with sensing and heating graphene layers. *Small* **10**, 3685 (2014).
79. **D. Jiang, Y. Wang, B. Li, C. Sun, Z. Wu, H. Yan, L. Xing, S. Qi, Y. Li, H. Liu, W. Xie, X. Wang, T. Ding, and Z. Guo**: Flexible sandwich structural strain sensor based on silver nanowires decorated with self-healing substrate. *Macromol. Mater. Eng.*, **304**, 1900074 (2019).
80. **Y. Li, T. Zhang, B. Jiang, L. Zhao, H. Liu, J. Zhang, J. Fan, Z. Guo, and Y. Huang**: Interfacially reinforced carbon fiber silicone resin via constructing functional nano-structural silver. *Compos. Sci. Technol.* **181**, 107689 (2019).
81. **S. Zhang, H. Liu, S. Yang, X. Shi, D. Zhang, C. Shan, L. Mi, C. Liu, C. Shen, and Z. Guo**: Ultrasensitive and highly compressible piezoresistive sensor based on polyurethane sponge coated with a cracked cellulose nanofibril/silver nanowire layer. *ACS Appl. Mater. Interfaces* **11**, 10922 (2019).
82. **C. Wang, M. Zhao, J. Li, J. Yu, S. Sun, S. Ge, X. Guo, F. Xie, B. Jiang, E.K. Wujcik, Y. Huang, N. Wang, and Z. Guo**: Silver nanoparticles/graphene oxide decorated carbon fiber synergistic reinforcement in epoxy-based composites. *Polymer* **131**, 263 (2017).
83. **Y. Guo, Y. Sun, Y.X. Wang, H. He, and Y.H. Zhu**: Thiol- and alkyne-functionalized copper nanoparticles as electrocatalysts for bisphenol A (BPA) oxidation. *J. Solid State Electrochem.* **23**, 91 (2019).
84. **X. Wang, X.B. Lu, L.D. Wu, and J.P. Chen**: 3D metal-organic framework as highly efficient biosensing platform for ultrasensitive and rapid detection of bisphenol A. *Biosens. Bioelectron.* **65**, 295 (2015).
85. **L. Zhu, L. Luo, and Z. Wang**: DNA electrochemical biosensor based on thionine-graphene nanocomposite. *Biosens. Bioelectron.* **35**, 507 (2012).
86. **M. Portaccio, D. Di Tuoro, F. Arduini, D. Moscone, M. Cammarota, D.G. Mita, and M. Lepore**: Laccase biosensor based on screen-printed electrode modified with thionine-carbon black nanocomposite, for bisphenol A detection. *Electrochim. Acta* **109**, 340 (2013).
87. **E. Dempsey, D. Diamond, and A. Collier**: Development of a biosensor for endocrine disrupting compounds based on tyrosinase entrapped within a poly(thionine) film. *Biosens. Bioelectron.* **20**, 367 (2004).
88. **Y. Zheng, D. Wang, Z. Li, X. Sun, T. Gao, and G. Zhou**: Laccase biosensor fabricated on flower-shaped yolk–shell SiO_2 nanospheres for catechol detection. *Colloids Surf., A* **538**, 202 (2018).
89. **C. Shan, H. Yang, D. Han, Q. Zhang, A. Ivaska, and L. Niu**: Water-soluble graphene covalently functionalized by biocompatible poly-L-lysine. *Langmuir* **25**, 12030 (2009).
90. **D. Jiang, V. Murugadoss, Y. Wang, J. Lin, T. Ding, Z. Wang, Q. Shao, C. Wang, H. Liu, N. Lu, R. Wei, A. Subramania, and Z. Guo**: Electromagnetic interference shielding polymers and nanocomposites—A review. *Polym. Rev.* **59**, 280 (2019).
91. **C. Wang, V. Murugadoss, J. Kong, Z. He, X. Mai, Q. Shao, Y. Chen, L. Guo, C. Liu, S. Angaiah, and Z. Guo**: Overview of carbon nanostructures and nanocomposites for electromagnetic wave shielding. *Carbon* **140**, 696 (2018).
92. **N. Wu, D. Xu, Z. Wang, F. Wang, J. Liu, W. Liu, Q. Shao, H. Liu, Q. Gao, and Z. Guo**: Achieving superior electromagnetic wave absorbers through the novel metal-organic frameworks derived magnetic porous carbon nanorods. *Carbon* **145**, 433 (2019).
93. **H. Gu, H. Zhang, C. Ma, H. Sun, C. Liu, K. Dai, J. Zhang, R. Wei, T. Ding, and Z. Guo**: Smart strain sensing organic–inorganic hybrid hydrogels with nano barium ferrite as the cross-linker. *J. Mater. Chem. C* **7**, 2353 (2019).
94. **H. Liu, Q. Li, S. Zhang, R. Yin, X. Liu, Y. He, K. Dai, C. Shan, J. Guo, C. Liu, C. Shen, X. Wang, N. Wang, Z. Wang, R. Wei, and Z. Guo**: Electrically conductive polymer composites for smart flexible strain sensors: A critical review. *J. Mater. Chem. C* **6**, 12121 (2018).
95. **Q. Li, H. Liu, S. Zhang, D. Zhang, X. Liu, Y. He, L. Mi, J. Zhang, C. Liu, C. Shen, and Z. Guo**: Superhydrophobic electrically conductive paper for ultrasensitive strain sensor with excellent anticorrosion and self-cleaning property. *ACS Appl. Mater. Interfaces* **11**, 21904 (2019).

https://doi.org/10.1557/jmr.2019.248 Published online by Cambridge University Press

© The Authors 2019